JMEPEG
https://doi.org/10.1007/s11665-023-08677-9

1059-9495/$19.00

ORIGINAL RESEARCH ARTICLE

Selection of Optimal Process Parameters to Obtain Defect-Free Builds in IN718 Made by Laser Powder Bed Fusion

Kurre Prasanth Kumar Reddy, Boggarapu Nageswara Rao, M.N. Nazeemudheen, Sushant K. Manwatkar, and S.V.S. Narayana Murty

Submitted: 23 April 2023 / Revised: 2 August 2023 / Accepted: 18 August 2023

This study investigates the effect of four major process variables viz. laser power, scanning speed, hatch distance and powder bed thickness on the densification behavior of Inconel 718 (IN718), with a view to obtain defect free builds during laser powder bed fusion (L-PBF) process. In order to determine the causes of defect generation, samples with different process variables were printed and examined microstructurally. Samples printed as per Taguchi's L9 orthogonal array have exhibited different types of microscopic defects such as porosity, lack of fusion (LOF) and cracks. Based on detailed study, the optimized process parameters for obtaining defect free IN718 builds were found to be with a laser power of 320 W at a scanning speed of 850 mm/s and a hatch distance of 0.11 mm. LOF and un-melted tracks have formed at low volume energy density (VED) while porosity was found at high VED values. Cracks are most evident in XZ plane, and the formation of such cracks is high at high laser power and scanning speed. Although VED represents the energy input to the process, it should no longer be considered a process parameter, as multiple combinations of input process variables with different performance characteristics can result in the same value. This aspect has been demonstrated in this paper with experimental data. A Modified Taguchi's approach has been followed in this study to develop empirical relationships to the performance characteristics (density), in terms of process variables and demonstrated their validity through comparison of test data. The method suggests few tests as per the orthogonal array and provides complete information for all combinations of levels and process variables. This method also provides the estimated range of output responses so that the scatter in the repeated tests can be assessed prior to the tests.

Keywords Additive manufacturing, inconel alloy IN718, laser powder bed fusion, Taguchi method

1. Introduction

The ability to maintain mechanical properties up to 650 °C coupled with good weldability makes nickel-based super alloy IN718, a candidate for high-temperature applications. The technology of additive manufacturing (AM) has great promise for 3D printing of parts with intricate, net or near net shapes, in short lead times, at a competitive cost, compared to conventional manufacturing.

Laser Powder bed fusion (L-PBF, a standard term defined in ASTM) is an AM process that uses a bed of powder with a source of heat to create metal parts and offers high design flexibility without the need for tooling. Near-net shaped engineering components can be built layer by layer using AM, which has distinct advantages of a low buy-to-fly ratio of close to about one, low lead time to manufacture the parts, at a competitive cost. This process is especially suitable for high cost materials like superalloys (IN718/IN625), titanium alloys (Ti-6Al-4V) and refractory alloys (C103), where the final parts are made by extensive and complicated machining necessitating high end computer numerical controlled machines, which involve both cost and time (Ref 1-3). Further improvements in redesign of the parts or assemblies through 'design for additive manufacturing' will facilitate weight reduction in printed parts, reduce or avoid weld joints, if any, making it more attractive from cost, time for realization, reduced inspection and reliability. AM is appealing to many modern manufacturing sectors, including aerospace, defense, energy, and automotive, where materials like nickel-based superalloys are difficult to fabricate using traditional subtractive methods (Ref 4). In order to enable their wider use, manufacturing of nickel-based superalloys using PBF has gained considerable attention. Being a process involving 'bottom-up' approach using metal powders through laser melting layer by layer, the builds inevitably contain microscopic defects such as porosity, LOF and cracks. Such defects can be controlled by maximizing density closer to 100% (Ref 5, 6). Therefore, the process variables affecting the build quality of part need to be carefully optimized to obtain defect free parts that could be successfully used for static, dynamic and shock loading conditions at both ambient and/or high/low temperatures. Therefore, it is

Kurre Prasanth Kumar Reddy and **Boggarapu Nageswara Rao**, Department of Mechanical Engineering, Koneru Lakshmaiah Education Foundation, Deemed to be University, Green Fields, Vaddeswaram, Guntur 522502, India; **M.N. Nazeemudheen**, Department of Mechanical Engineering, National Institute of Technology Calicut, Calicut 673601, India; **Sushant K. Manwatkar**, Materials and Mechanical Entity, Vikram Sarabhai Space Centre, Trivandrum 695022, India; and **S.V.S. Narayana Murty**, Materials and Manufacturing Entity, Liquid Propulsion Systems Centre, Trivandrum 695022, India. Contact e-mail: kprasanthkumarreddy@gmail.com.

Published online: 05 September 2023

essential to understand the effect of process variables on the evolution of defects and effect of defects on the properties of materials (Ref 7-10).

During L-PBF process, a laser beam is used to selectively melt a thin layer of metal powder in the shape of the cross section of the desired final part (Ref 11, 12). After each layer is fused, the build platform is lowered, and a new layer of powder is spread, and the process is continued till the complete part is printed. Caiazzo et al. (Ref 13) recently studied the relevance of VED during the investigation of IN718 in LPBF. They explained technological and mechanical properties of AM parts such as roughness, hardness, size and number of pores as well as fractional density in terms of VED useful to the designers as a function of process parameters.

In L-PBF systems, there are many process variables, the most commonly considered being laser power, P(W), scanning speed, SS (mm/s), layer thickness, LT (mm), distance between consecutive laser passes and hatch distance, HD (mm). Optimized process parameters are empirically derived to produce dense builds, minimize defects, reduce surface roughness, increase build speed, and produce parts with acceptable material properties (Ref 14). As there are infinite options for a given part design, it is impossible to have one set of parameters that will be fully optimized for all part features (such as thin walls, thick sections, overlaps, or others), material performance, and process productivity. In view of this, generic parameter sets are developed to accommodate as many priorities as possible and build geometries. However, significant opportunities remain for further optimization of specific parts, geometries and applications. In addition, optimized parameters are constantly changing even for the same material, as manufacturers introduce new machine models and technologies, and processes continue to evolve. An excellent review by Deb Roy et al. (Ref 15) is available which provides details of the mechanisms of most build-related issues (porosity, residual stress, preferential evaporation, among others), grain morphology and texture developed during the L-PBF process.

Many researchers adopted Taguchi method utilizing the Minitab software without validation of the complete generated test data. They compare only the optimal solution with the average of the repeated test data. Modified Taguchi approach provides optimal solution and recommends the development of an empirical relation for the output response in terms of input process variables (in non-dimensional form) using the additive law and ANOVA results. In this case, there is no need to use Minitab software. It provides the range of estimates for the output response (useful in case of repeated tests) for all level combinations of the input process variables.

In the present work, using the L-PBF method, experiments have been carried out to produce builds by monitoring a performance indicator (such as density) and defining a set of processing parameters (such as P, SS and HD) to obtain a small number of test data and provide the information/data needed for an experiment with a full factorial design, using the modified Taguchi approach. Empirical relationships have been established for the process parameters based performance indicator.

2. Experimental

Gas atomized Inconel 718 powder supplied by EOS GmbH (Krailling, Germany) was used to print the samples. The chemical composition of the material is (all in wt.%): 53.35 Ni, 19.15 Cr, 4.99 Nb, 3.19 Mo, 1.1 Ti, 0.48 Al and Balance Fe. Measurements were made by inductively coupled plasma atomic emission spectroscopy (ICP-AES). The L-PBF machine (EOSINT M280_400 W) equipped with a single continuous wave fiber laser, was employed to print cubic samples of IN718 with dimensions of 10 mm × 10 mm × 5 mm. All samples were printed on an IN718 substrate pre-heated to 100 °C. The most influential processing parameters including P, SS were varied independently to examine the formation of defects and microstructures. Table 1 gives the AM process parameters used in the present experimentation. Using Taguchi's L9 orthogonal array, 9 samples were printed with 3 levels of P (W) (240, 320, 400) and SS (mm/s) (300, 850, 400) at constant HD of 0.11 mm and LT of 0.04 mm and an empirical relationship has been established. In order to validate the developed empirical relation, more samples were printed at varying laser power (levels-240, 320, 400,all in W), SS (levels-300, 410, 520, 630, 740, 850, 960, 1070, 1180, 1290, 1400 (all in mm/s) at constant HD of 0.11 mm and LT of 0.04 mm.

Table 1 3D print process parameters used in the present study

Process parameter	Units	Range
Laser power (P)	W	240-400
Scanning speed (SS)	mm/s	300-1400
Hatch distance (HD)	mm	0.11
Layer thickness (LT)	mm	0.04

The builds were prepared in a chamber purged with argon gas, and oxygen content was maintained below 0.1 % to control gas pickup. To minimize the thermal stresses during the building process, a meander scanning pattern was adopted for each layer deposition. The scanning direction was rotated by 67° between the adjacent deposition layers. The scan strategy is the tool path that the lasers take during part making.

In order to examine the effect of VED on the density, more test samples were printed at a VED of 67.5 J/mm^3, by varying *P* and SS with hatch distance of 0.11 mm and layer thickness of 0.04 mm. In addition, a few more samples were printed at a VED of 67.5 J/mm^3 varying *P* and HD with SS of 960 mm/s.

After fabrication, the samples were removed from the substrate without performing any stress relieving operation. Density measurements of the printed samples were conducted via Archimedes' method, pursuant to ASTM B962-17. The microstructures were examined using an optical microscope (OLYMPUS GX71) and scanning electron microscope (SEM) (Carl Zeiss EVO 50) to study the nature of defects and microstructures. The samples were cross sectioned parallel to the build direction (XZ) and perpendicular to the build direction (XY), with the *z*-axis along the build direction. For metallographic examination, the samples were polished using conventional metallography practices, using a series of emery papers and final polishing was performed using diamond paste of one micron size. The freshly polished specimens were etched using an etchant consisting of hydrochloric acid (HCl), copper chloride ($CuCl_2$), ethanol and nitric acid (HNO_3) for 20-30 s.

The freshly polished and etched samples were subjected to hardness measurements. The process for determining Vickers hardness in XY and XZ planes is as follows. In XZ plane a total of 20 and in XY plane a total 16 Hardness values were obtained

from four equidistant lines along the X direction, with each line contributing 5 and 4 values, respectively. A load of 300 gf was applied for 13 s dwell time and measurements were obtained.

3. Theoretical Considerations

3.1 Energy Density

In additive manufacturing, energy density (ED) establishes how much energy can be imparted to a given volume of material, in a given period of time. Utilizing this energy, materials are fused, sintered, or layered to form solid objects. Faster production times and stronger finished parts are often associated with higher ED. Variables must be chosen for the intended AM process, in such a way that the material is completely melted and fused resulting in defect-free part geometries. Overall, the ED in additive manufacturing is a tool that aids in ensuring the properties of the printed object.

Jiang et al. (Ref 16) have followed the concept of equivalent energy density (E_0) which is a function of several parameters. Among them, three important input process variables, viz., P, SS and HD were selected and represented as Eq 1. Specifying these three input process variables, the performance indicators were evaluated and plotted with E_0. Plots showed large scatter and it was not possible to correlate the performance indicator explicitly with E_0. This is due to the fact that E_0 can have a value for multiple combinations of input process variables with different values of the performance indicator. Several researchers have extensively employed the concept of ED (Ref 17-20), while some have specifically referred to it as VED (Eq 1) (Ref 21-25).

$$\mathrm{ED} = \mathrm{VED} = \frac{\mathrm{P}}{\mathrm{SS} \times \mathrm{HD} \times \mathrm{LT}} \qquad \text{(Eq 1)}$$

Factors that can affect the VED include P, SS, HD and LT. Generally, IN718 requires efficient melting and solidification during the manufacturing process, which results in strong and dense parts with good mechanical properties. Following the Taguchi's L_9 orthogonal array (OA), the samples were printed at 0.11 mm HD and 0.04 mm LT with P varying from 240 to 400 W and SS varying from 300 to 1400 mm/s. From the measured density of L-PBF processed IN718 samples, the relative density (Eq 2) was calculated using the following relation (Ref 26).

$$\text{Relative Density} = \left(\frac{\text{Density calculated (Archimedes Principle)}}{\text{Theoritical Density of material}}\right) \times 100 \qquad \text{(Eq 2)}$$

The theoretical density of IN718 is taken as 8.2 g/cc.

3.2 Modified Taguchi Approach

For 4 process parameters with 3 assigned levels to each parameter, the minimum test runs (N_{Taguchi}) required is (Ref 27)

$$N_{\mathrm{Taguchi}} = 1 + n_p \times (n_l - 1) = 1 + 4 \times (3 - 1) = 9 \qquad \text{(Eq 3)}$$

Here, n_p is the number of process parameters. n_l, is the number of levels assigned to each process parameter. Equation 3 indicates the selection of L_9 OA as more appropriate. For L_9 OA, substitution of the number of test runs, $N_{\mathrm{Taguchi}} = 9$ and the levels, $n_l = 3$ in Eq 3, one can find n_p=4. That means 4 factors can be accommodated in 9 test runs. As in (Ref 28-31) Table 2 provides the levels of L-PBF process parameters (viz., P, SS) and the fictitious parameters (f_1 and f_2). Table 3 gives the test data of the performance indicator (viz., density) of the 9 samples as per the Taguchi's L_9 OA. Analysis of variance (ANOVA) results and the significance of L-PBF process parameters are presented in Table 4. It is seen that percentage of contribution of P, SS, and the fictitious parameters f_1 and f_2 on the density are 2.56%, 94.07%, 2.31%, and 1.06% respectively. The percentage contribution of f_1 and f_2 on the density (2.31% and 1.06%) is nothing but the error (%).

4. Results and Discussion

4.1 Development of an Empirical Relation

Additive law provides the estimates of the performance indicator (viz., density) from the mean values of ANOVA (Table 4). The evaluation procedure for the estimates of the performance indicator is explained below. Let ρ be the density (performance indicator) and $\hat{\rho}$ is its estimate for the L-PBF process parameters (P_i, SS_j) varying the subscripts i, j from 1 to 3. $\rho(P_i)$ and $\rho(\mathrm{SS_j})$ are designated as the mean values of ρ to the i^{th} level of P and the j^{th} level of SS. The grand mean of ρ is designated by ρ_{mean} for the 9 test runs. Following the additive law, estimate $\hat{\rho}$ for the specified (P_i, SS_j) is:

$$\hat{\rho} = \rho(P_i, \mathrm{SS}_j) = \rho(P_i) + \rho(\mathrm{SS}_j) - \rho_{\mathrm{mean}} \qquad \text{(Eq 4)}$$

Table 5 provides estimates of the density, $\hat{\rho}$(g/cc) from the mean values in ANOVA Table 4 using additive law (Eq 4). Grand mean, $\rho_{\mathrm{mean}} = 7.9773\mathrm{g/cc}$. The discrepancy between estimates and the test data is within 1%.

Deviations in density (ρ) from the mean values of the fictitious parameters f_1 and f_2 over the grand mean (ρ_{mean}) were obtained from:

$$\Delta\rho_{ij} = \rho(f_{ij}) - \rho_{\mathrm{mean}} \quad \forall \mathrm{i},\ \mathrm{j} = 1 \text{ to } 3 \qquad \text{(Eq 5)}$$

For example, $\Delta\rho_{11} = \rho(f_{11}) - \rho_{\mathrm{mean}} = 7.9363 - 7.9773 = -0.0410$. Similarly, other deviations in density can be found from the ANOVA Table 4.

Corrections $\Delta\rho_-$ and $\Delta\rho_+$ to the estimates from the additive law (Eq 4) were made for obtaining lower and upper bounds as:

$$\begin{aligned}\Delta\rho_- &= \min\{\Delta\rho_{11}, \Delta\rho_{12}, \Delta\rho_{13}\} + \min\{\Delta\rho_{21}, \Delta\rho_{22}, \Delta\rho_{23}\} \\ &= \min\{-0.0410,\ 0.0190,\ 0.0220\} \\ &\quad + \min\{-0.0193, 0.0270,\ -0.0077\} \\ &= -0.0410 - 0.0193 = -0.0603\end{aligned} \qquad \text{(Eq 6)}$$

$$\begin{aligned}\Delta\rho_+ &= \max\{\Delta\rho_{11}, \Delta\rho_{12}, \Delta\rho_{13}\} + \max\{\Delta\rho_{21}, \Delta\rho_{22}, \Delta\rho_{23}\} \\ &= \max\{-0.0410,\ 0.0190,\ 0.0220\} \\ &\quad + \max\{-0.0193, 0.0270,\ -0.0077\}\end{aligned} \qquad \text{(Eq 7)}$$

Applying the corrections $\Delta\rho_- = -0.0603$ and $\Delta\rho_+ = 0.049$ to the density obtained from the additive law (Eq 4), one can find the expected range of the density. Table 6 gives the expected range of density for the 9 test runs. The test data is

Table 2 Levels of L-PBF process parameters at 0.11 mm hatch distance and 0.04 mm layer thickness

L-PBF process parameters	Designation	Level-1	Level-2	Level-3
Laser power, *P*, W	P	240	320	400
Scanning speed, SS, mm/s	SS	300	850	1400
Fictitious parameter	f_1	f_{11}	f_{12}	f_{13}
Fictitious parameter	f_2	f_{21}	f_{22}	f_{23}

Table 3 Test data of the performance indicator (viz., density) of 9 samples as per the Taguchi's L9 OA

	Levels of L-PBF process parameters				L-PBF process parameters		Fictitious parameters		
Test run	Laser power, *P*, W	Scanning speed, SS (mm/s)			f_1	f_2			Density, ρ, g/cc
Laser power, *P*, W	Scanning Speed, SS, mm/s	f_1		f_2					
1	1	1	1	1	240	300	f_{11}	f_{21}	7.618
2	1	2	2	2	240	850	f_{12}	f_{22}	8.145
3	1	3	3	3	240	1400	f_{13}	f_{23}	8.050
4	2	1	2	3	320	300	f_{12}	f_{23}	7.764
5	2	2	3	1	320	850	f_{13}	f_{21}	8.176
6	2	3	1	2	320	1400	f_{11}	f_{22}	8.096
7	3	1	3	2	400	300	f_{13}	f_{22}	7.772
8	3	2	1	3	400	850	f_{11}	f_{23}	8.095
9	3	3	2	1	400	1400	f_{12}	f_{21}	8.080

Table 4 ANOVA and the significance of L-PBF process parameters on the density

L-PBF parameters	1-mean	2-mean	3-mean	Sum of squares (SOS)	%Contribution
Density, ρ (g/cc); grand mean = 7.9773					
Laser power, *P*, W	7.9377	8.0120	7.9823	8.40E−03	2.56
Scanning speed, SS, mm/s	7.7180	8.1387	8.0753	3.09E−01	94.07
f_1	7.9363	7.9963	7.9993	7.58E−03	2.31
f_2	7.9580	8.0043	7.9697	3.48E−03	1.06

Table 5 Estimates of the density from the mean values in ANOVA (Table 4) using additive law (4)

	L-PBF process parameters		Mean values of density, ρ from ANOVA Table 4			Density (g/cc)		
Test run $\rho(P_i)$	Laser power, *P* (W) $\rho(SS_j)$	Scanning speed, SS (mm/s) Additive law (4)	Test			(i^{th}, j^{th})		Relative error, R.E. (%)
1	240	300	(1, 1)	7.9377	7.7180	7.678	7.618	− 0.79
2	240	850	(1, 2)	7.9377	8.1387	8.099	8.145	0.56
3	240	1400	(1, 3)	7.9377	8.0753	8.036	8.050	0.18
4	320	300	(2, 1)	8.0120	7.7180	7.753	7.764	0.15
5	320	850	(2, 2)	8.0120	8.1387	8.195	8.176	− 0.24
6	320	1400	(2. 3)	8.0120	8.0753	8.110	8.096	− 0.17
7	400	300	(3, 1)	7.9823	7.7180	7.745	7.772	0.35
8	400	850	(3, 2)	7.9823	8.1387	8.144	8.095	− 0.60
9	400	1400	(3, 3)	7.9823	8.0753	8.080	8.080	0.00

found to be within/close to the lower bound value $(\widehat{\rho} + \Delta\rho_{-})$ and the upper bound value $(\widehat{\rho} + \Delta\rho_{+})$. In fact, additive law (Eq 4) estimates the density for all combinations of the L-PBF process parameters. Empirical relation for the density in terms of L-PBF process parameters is required for estimating the density throughout the range of the parameters.

Table 6 Expected range of density for the test runs in Taguchi's L9 OA

	L-PBF process parameters			Estimated density, g/cc		
Test run	Laser power, *P* (W)	Scanning speed, SS (mm/s)	Testdensity, ρ (g/cc)	Additivelaw (4)	Lower bound	Upper bound
1	240	300	7.618	7.678	7.618	7.727
2	240	850	8.145	8.099	8.039	8.148
3	240	1400	8.050	8.036	7.975	8.085
4	320	300	7.764	7.753	7.692	7.802
5	320	850	8.176	8.195	8.135	8.244
6	320	1400	8.096	8.110	8.050	8.159
7	400	300	7.772	7.745	7.685	7.794
8	400	850	8.095	8.144	8.083	8.193
9	400	1400	8.080	8.080	8.020	8.129

Empirical relation is developed for the density (ρ) in terms of *P* and SS using the additive law from the mean values of ANOVA.

$$\rho = 8.1733 + 0.0223\xi_1 - 0.052\xi_1^2 + 0.1787\xi_2 - 0.242\xi_2^2 \quad \text{(Eq 8)}$$

Here, $\xi_1 = \frac{1}{80}(P - 320)$ and $\xi_2 = \frac{1}{550}(SS - 850)$.

Estimations in Table 7, 8, 9 are from the developed empirical relation (Eq 8) by varying *P* from 240 to 400 W; SS from 300 to 1400 mm/s at constant HD of 0.11 mm and LT of 0.04 mm. The test data is found to be within the estimated range.

Figure 1(a) compares the density using additive law and test data. Figure 1(b) shows test data of density in between the estimated range (upper bound and lower bound), which clearly indicates the adequacy of the developed empirical relation (Eq 8). From the ANOVA Table 4, the maximum density is expected for the set of L-PBF processing parameters (P_2, SS_2) in which the subscripts denote the level of the process parameters.

In the present study, the optimal L-PBF process parameters to achieve maximum density are the laser power, $P_2 = 320$W and the scanning speed, $SS_2 = 850$mm/s which correspond to the test run-5 in Table 3 of the Taguchi's L_9 OA, and the achieved density, $\rho_{max} = 8.176\,g/cc$. The additive law (Eq 4) estimates the maximum density, $\rho_{max} = 8.195\,g/cc$, and the expected range is from 8.135 to 8.244 g/cc. The test data is within the expected range. Since, percentage contribution of SS is high, the variation of density with scanning speed is shown in Fig. 1(c) at a constant laser power (320 W). The variation of density with laser power in Fig. 1(d) is for 850 mm/s scanning speed. All estimates of the density including test data were made for all possible combinations of L-PBF process parameters. Variation of measured density with VED considering complete test data is presented in Fig. 2. The large scatter in density with VED (seen in Fig. 2(a)) is mainly attributed to different sets of L-PBF process parameters which yield a given VED value. This should not be treated as an experimental scatter. The dispersion in density for VED of 67.5 J/mm^3 is clearly visible in Fig. 2(b).

4.2 Effect of L-PBF Process Parameters

The effect of L-PBF process parameters on the microstructure and densification of IN718 were examined here in detail. Above 99% densification was achieved for 360 W of P and the range of SS.

For a SS of 960 mm/s, the melt pool depth has increased, whereas width has decreased with laser power. For a *P* of 360 W, as the melt pool depth decreased, and width increased relatively with scanning speed. Conduction mode, transition mode and keyhole conduction modes are possible in case of additive manufacturing. Table 10 shows the densification of the printed builds and the estimated range with actual test data.

The process parameters, such as P and SS, play a crucial role in determining the quality and properties of the printed parts. The variation in density observed in this study is attributed to the changes in the L-PBF process parameters. By increasing the *P*, more energy is delivered to the powder bed, resulting in a deeper melt pool. Conversely, by increasing the SS, the width of the melt pool decreases. Therefore, the combination of higher laser power and lower SS leads to an increased melt pool depth-to-width ratio. Figure 3 showcases a montage of optical microstructures of specimens that were printed using different combinations of *P* and SS under the experimental conditions studied. These microstructures provide visual evidence of the effect of process parameters on the resulting material density.

To further understand the relationship between process parameters and build quality, Table 12 presents the densification results of specimens at a constant VED, while varying the laser power and hatch distance. Table 12 highlights how the process parameters impact the achieved density of the 3D printed parts. It emphasizes the dependency of build quality on these specific process parameters, indicating that adjusting laser power and hatch distance can lead to variations in densification. It emphasizes the significance of optimizing laser power, scanning speed, and hatch distance to ensure consistent and controlled fabrication of defect-free parts.

The VED in Eq 1 consists of the L-PBF process parameters (P, SS, HD and LT). For any specific VED value, it is possible to create many sets of the L-PBF process parameters. An attempt is made to obtain the densification for the created sets of the L-PBF process parameters to examine the influence of VED. Table 11 and 12 give the achieved densification for the created sets of L-PBF process parameters for which VED = 67.5 J/mm^3. It is clearly visible that for a constant value of VED = 67.5 J/mm^3, appreciable variation in the densification is observed. This variation is not due to the experimental scatter. It is mainly due to the variation in the sets of the L-PBF process parameters. Hence the densification cannot be represented explicitly in terms of VED. Since, there are 4 L-PBF process parameters, two case studies were made. In the first case, two parameters (*P* and SS) are varied by keeping HD and

Table 7 Estimates of the density, by varying SS (300 to 630 mm/s)

Laser power, *P* (W)	Scanning speed, SS (mm/s)	VED (J/mm^3) Eq 1	Density, ρ (g/cc)	Relative density (%)Eq 2	Estimates of density, ρ (g/cc)		
					Empirical relation Eq 8	Lower bound	Upper bound
240	300	181.82	7.618	92.90	7.678	7.618	7.727
280	300	212.12	7.613	92.84	7.728	7.668	7.777
320	300	242.42	7.764	94.68	7.753	7.692	7.802
360	300	272.73	7.797	95.09	7.751	7.690	7.800
400	300	303.03	7.772	94.78	7.723	7.663	7.772
240	410	133.04	7.880	96.10	7.801	7.741	7.850
280	410	155.21	7.798	95.10	7.851	7.791	7.900
320	410	177.38	7.848	95.71	7.875	7.815	7.924
360	410	199.56	7.872	96.00	7.874	7.813	7.923
400	410	221.73	7.827	95.45	7.846	7.785	7.895
240	520	104.90	8.107	98.87	7.905	7.844	7.954
280	520	122.38	8.096	98.73	7.955	7.895	8.004
320	520	139.86	8.004	97.61	7.979	7.919	8.028
360	520	157.34	7.983	97.35	7.977	7.917	8.026
400	520	174.83	8.024	97.85	7.949	7.889	7.998
240	630	86.58	8.041	98.06	7.989	7.929	8.038
280	630	101.01	8.122	99.05	8.039	7.979	8.088
320	630	115.44	8.180	99.76	8.063	8.003	8.112
360	630	129.87	8.118	99.00	8.061	8.001	8.110
400	630	144.30	8.111	98.91	8.033	7.973	8.082

Table 8 Estimates of the density, by varying SS (740 to 960 mm/s)

Laser power, *P* (W)	Scanning speed, SS (mm/s)	VED (J/mm^3) Eq 1	Density, ρ (g/cc)	Relative density (%) Eq 2	Estimates of density, ρ (g/cc)		
					Empirical relation Eq 8	Lower bound	Upper bound
240	740	73.71	7.995	97.50	8.054	7.993	8.103
280	740	86.00	7.993	97.48	8.104	8.043	8.153
320	740	98.28	8.207	100.09	8.128	8.068	8.177
360	740	110.57	8.193	99.91	8.126	8.066	8.175
400	740	122.85	8.138	99.24	8.098	8.038	8.147
240	850	64.17	8.145	99.33	8.099	8.039	8.148
280	850	74.87	8.069	98.40	8.149	8.089	8.198
320	850	85.56	8.176	99.71	8.173	8.113	8.222
360	850	96.26	8.253	100.65	8.171	8.111	8.220
400	850	106.95	8.095	98.72	8.144	8.083	8.193
240	960	56.82	8.035	97.99	8.125	8.065	8.174
280	960	66.29	8.096	98.73	8.175	8.115	8.224
320	960	75.76	8.105	98.84	8.199	8.139	8.248
360	960	85.23	8.141	99.28	8.198	8.137	8.247
400	960	94.70	8.165	99.57	8.170	8.109	8.219

LT at constant. In the second case, two parameters (*P* and HD) are varied by keeping SS and LT constant.

Although energy density represents the energy input to the process, it should no longer be considered a process parameter. It can have a value for multiple combinations of input process variables with different performance characteristics. This aspect is demonstrated in this paper with test data. Modified Taguchi's method has been followed to develop empirical relationships to the performance characteristics in terms of process variables and demonstrated their validity through comparison of test data. The method suggests few tests as per the orthogonal array and provides complete information for all combinations of levels and process variables. The method also provides the estimated range of output responses so that the scatter in the repeated tests can be assessed prior to the tests.

4.3 Microstructural Observations

The L-PBF process has a significant advantage in terms of producing complex parts with high material utilization. However, it is influenced by several factors, including laser power,

Table 9 Estimates of the density, by varying SS (1070 to 1400 mm/s)

Laser power, P (W)	Scanning speed, SS (mm/s)	VED, J/mm^3 Eq 1	Density, ρ (g/cc)	Relative density (%) Eq 2	Estimates of density, ρ (g/cc)		
					Empirical relation Eq 8	Lower bound	Upper bound
240	1070	50.98	8.073	98.45	8.132	8.071	8.181
280	1070	59.47	8.054	98.22	8.182	8.122	8.231
320	1070	67.97	8.139	99.26	8.206	8.146	8.255
360	1070	76.47	8.153	99.43	8.204	8.144	8.253
400	1070	84.96	8.098	98.76	8.176	8.116	8.225
240	1180	46.22	8.109	98.89	8.119	8.059	8.168
280	1180	53.93	8.115	98.96	8.169	8.109	8.218
320	1180	61.63	8.109	98.89	8.193	8.133	8.242
360	1180	69.34	8.108	98.88	8.192	8.131	8.241
400	1180	77.04	8.118	99.00	8.164	8.103	8.213
240	1290	42.28	8.087	98.62	8.087	8.027	8.136
280	1290	49.33	8.046	98.12	8.137	8.077	8.186
320	1290	56.38	8.133	99.18	8.161	8.101	8.210
360	1290	63.42	8.133	99.18	8.160	8.099	8.209
400	1290	70.47	8.117	98.99	8.132	8.071	8.181
240	1400	38.96	8.050	98.17	8.036	7.975	8.085
280	1400	45.45	8.153	99.43	8.086	8.026	8.135
320	1400	51.95	8.096	98.73	8.110	8.050	8.159
360	1400	58.44	8.128	99.12	8.108	8.048	8.157
400	1400	64.94	8.080	98.54	8.080	8.020	8.129

scanning speed, hatch distance, scan strategy, powder material, powder size, and morphology (Ref 32), absorption and transmission of laser energy, rapid melting and solidification of material, microstructure evolution, and materials evaporation (Ref 33), which are all part of the L-PBF process. The presence of microscopic defects can affect the mechanical properties of the fabricated part (Ref 34-36).

Lack-of-fusion (LOF) refers to a defect where there is incomplete fusion between the base layer and new layer. This can result in compromising the structural integrity of the component. As shown in optical photomicrographs, the quality of printed parts can be assessed from various types of defects, including LOF. In Fig. 4(a), the optical micrograph shows a horizontal lack of fusion (H-LOF). This indicates that there is incomplete fusion along the horizontal plane between the adjacent areas. The image displays a visible region where fusion is not adequately achieved. The H-LOF defect can be problematic in applications where the part is subjected to significant loads. In Fig. 4(b), the optical micrograph shows a vertical lack of fusion (V-LOF). This suggests that there is incomplete fusion along the built plane between the base layer and new layer. Similar to H-LOF, V-LOF can result in compromised structural integrity. The image reveals a lack of bonding/gap in the fusion region along the vertical axis.

By visualizing these optical micrographs, quality of builds can be assessed from the types of defects present. This information is valuable for ensuring the reliability and performance of the printed parts. Corrective actions can then be taken to rectify the LOF issues, by adjusting process parameters.

The LOF defects form because the metal powders are not fully melted enough to deposit a new layer on top of the previous one. Figure 5(a) shows the LOF, and Fig. 5(b) shows LOF scanning track in XY Plane. LOF may be considered as (i) poor bonding defects caused by a lack of molten metal during the solidification process, as shown in Fig. 6(a) and (ii) defects caused by un-melted metal powders, as shown in Fig. 6(b). When the laser energy is insufficient to cause sufficient molten pool penetration, interlayer bonding defects form. As a result, LOF defects are commonly found in the scan tracks and deposited layers. In a continuous deposition process, interlayer defects may gradually extend and propagate upwards to form large multi-layer defects.

The optical micrograph in Fig. 7(a) shows LOF due to deficiency in remelting of melt pools and Fig. 7(b) shows deficiency in fusing of scanning tracks. Crack initiation and propagation in fabricated parts are caused by a high temperature gradient combined with large residual stresses (Ref 37, 38). Figure 8(a) and (b) shows the formation of inter-layer cracks with delamination. Intra-layer cracks are formed in a layer during solidification of the melt pool between the solidified layer and the printed layer (Fig. 9(a)). Shrinkage and residual stresses in the melt pool causes intra-layer cracks (Fig. 9(b)). Intra-layer cracks have a shorter length because they typically form within the melt pool's dimensions. The density, range and test data for the samples identified with significant defects is presented in Table 13. The introduction of undesirable thermal residual stresses, LOF porosities during the process are unavoidable. Some experimental trails were made to correlate the porosity fraction with the melt pool geometry and L-PBF process parameters (Ref 39-41). However, the influence of porosities on density of the realized parts needs special attention for quantification.

In this paper, the L-PBF process parameters (viz., P, SS and HD) were identified for IN718 powder to achieve maximum density (ρ). It may be noted that for each value of VED, it is possible to have multiple combinations of input process parameters. Hence different performance indicators can be expected for each combination of input process parameters. This implies that different values of the performance indicators for each VED are not due to experimental scatter. Modified

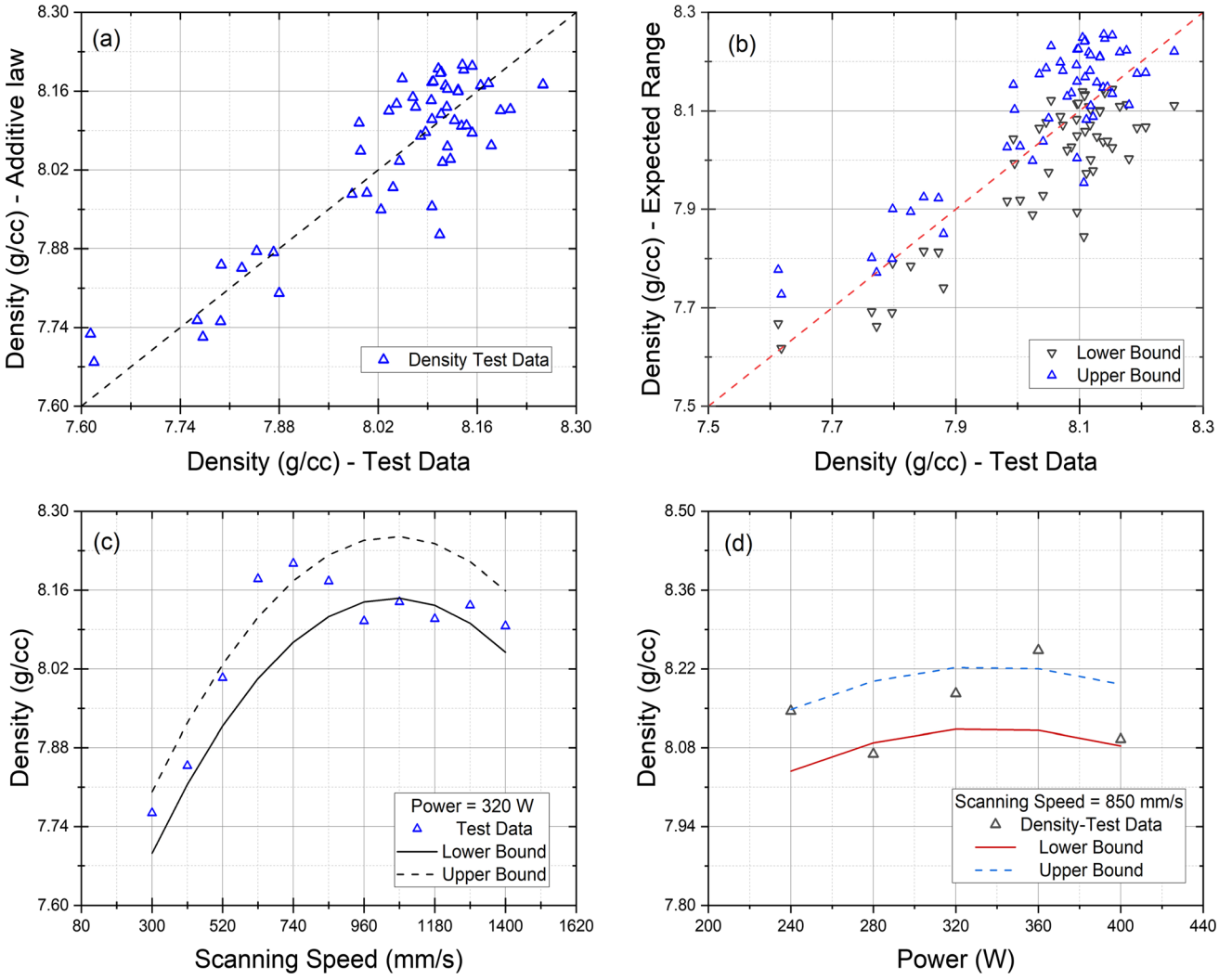

Fig. 1 (a) comparison of density estimates with the test data; (b) comparison of density test data with estimates; (c) variation of density with SS of 320W *P* at HD of 0.11 mm and LT of 0.04 mm and (d) variation of density with *P* of 850 mm/s SS at HD of 0.11 mm and LT of 0.04 mm

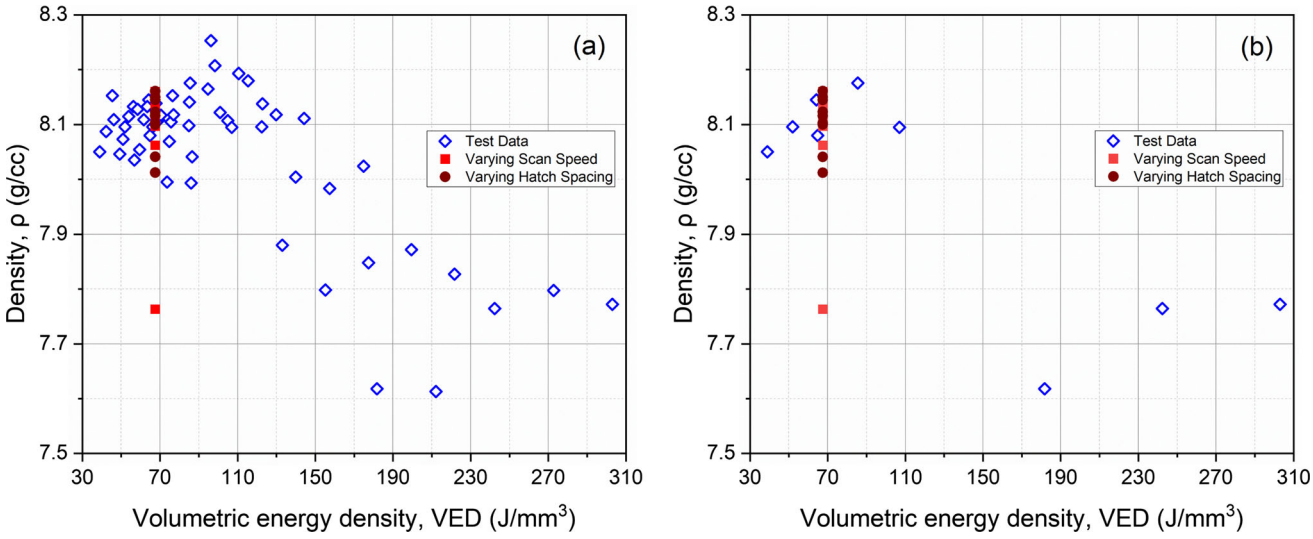

Fig. 2 (a) Variation of density with VED for all test data and (b) variation of density with VED from the data of L9 orthogonal array

Table 10 Densification of the printed builds and the estimated range with test data of IN718 for the specified *P* (W) and SS (mm/s)

SS*P*	300	520	740	960	1180	1400
240	7.618-7.727 (7.618)*	7.844-7.954 (8.107)	7.993-8.103 (7.995)	8.065-8.174 (8.035)	8.059-8.168 (8.109)	7.975-8.085 (8.05)
280	7.668-7.777 (7.613)	7.895-8.004 (8.096)	8.043-8.153 (7.993)	8.115-8.224 (8.096)	8.109-8.218 (8.115)	8.026-8.135 (8.153)
360	7.690-7.800 (7.797)	7.917-8.026 (7.983)	8.066-8.175 (8.193)	8.137-8.247 (8.141)	8.131-8.241 (8.108)	8.048-8.157 (8.128)
400	7.663-7.772 (7.772)	7.889-7.998 (8.024)	8.038-8.147 (8.138)	8.109-8.219 (8.165)	8.103-8.213 (8.118)	8.020-8.129 (8.08)

*Figure 3 test data.

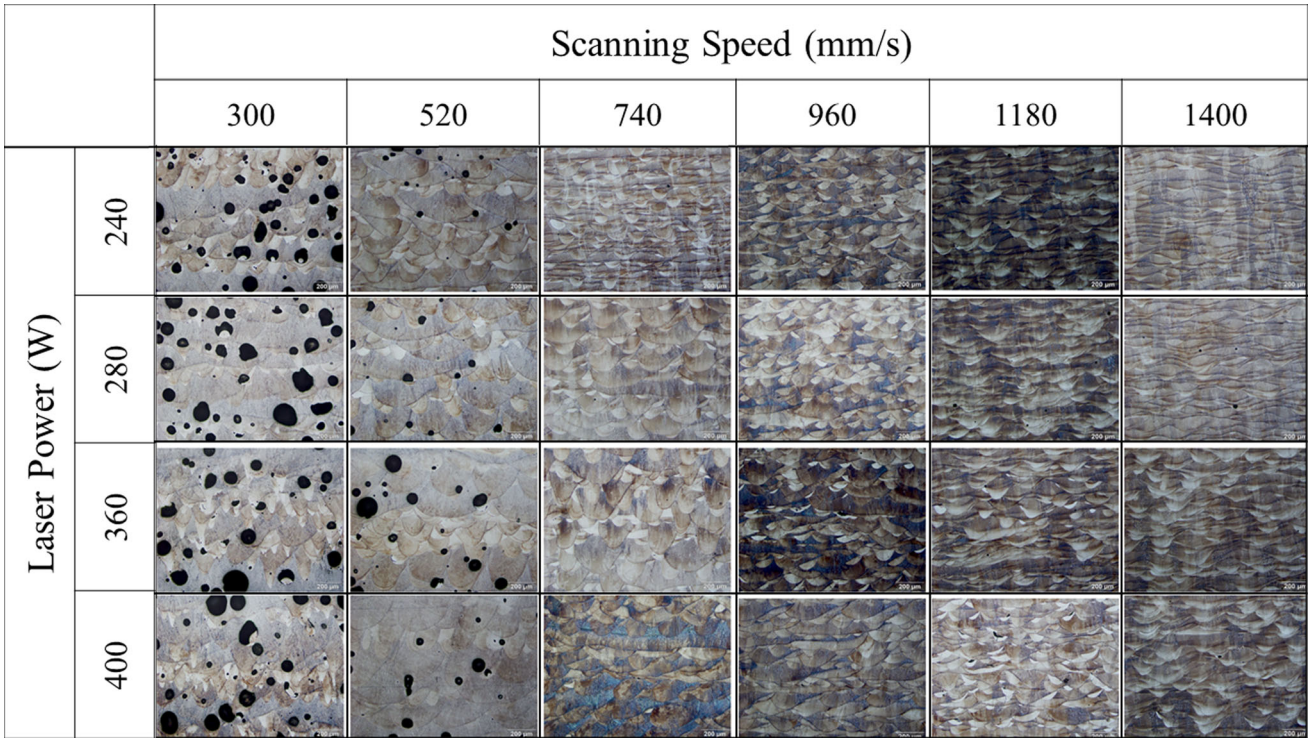

Fig. 3 Montage of optical microstructures of specimens printed using various scan power and scanning speed at all experimental conditions studied

Table 11 Density for a constant VED, HD of 0.11 mm and LT of 0.04 mm

L-PBF process parameters			Density, g/cc	
Laser power, *P* (W)	Scanning speed, SS (mm/s)	VED, J/mm^3	Test	Estimated range
240	808	67.5	8.103	8.024-8.133
260	876	67.5	8.12	8.075-8.184
280	943	67.5	8.16	8.112-8.221
300	1011	67.5	8.108	8.136-8.245
320	1078	67.5	8.101	8.145-8.255
340	1145	67.5	7.763	8.142-8.251
360	1213	67.5	8.062	8.124-8.233
380	1280	67.5	8.097	8.092-8.202
400	1347	67.5	8.136	8.047-8.156

Taguchi approach has been adopted by considering the data of few tests and data has been generated for the full factorial design of experiments. ANOVA has been performed to assess the significance of the L-PBF process parameters on density. Test results are found to be close to the expected range of density. The developed empirical relations can be used for

Table 12 Density for a constant VED and LT of 0.04 mm

L-PBF process parameters				Density, g/cc	
Laser power, *P* (W)	Scanning speed, SS (mm/s)	Hatch distance, HD (mm)	VED, J/mm^3	Test	Range
240	960	0.0926	67.5	8.15	8.053-8.163
260	960	0.1	67.5	8.103	8.052-8.162
280	960	0.1081	67.5	8.1	8.049-8.158
300	960	0.1158	67.5	8.012	8.042-8.151
320	960	0.1235	67.5	8.161	8.032-8.141
340	960	0.1312	67.5	8.116	8.019-8.128
360	960	0.139	67.5	8.145	8.003-8.112
380	960	0.1467	67.5	8.041	7.984-8.093
400	960	0.1544	67.5	8.123	7.962-8.071

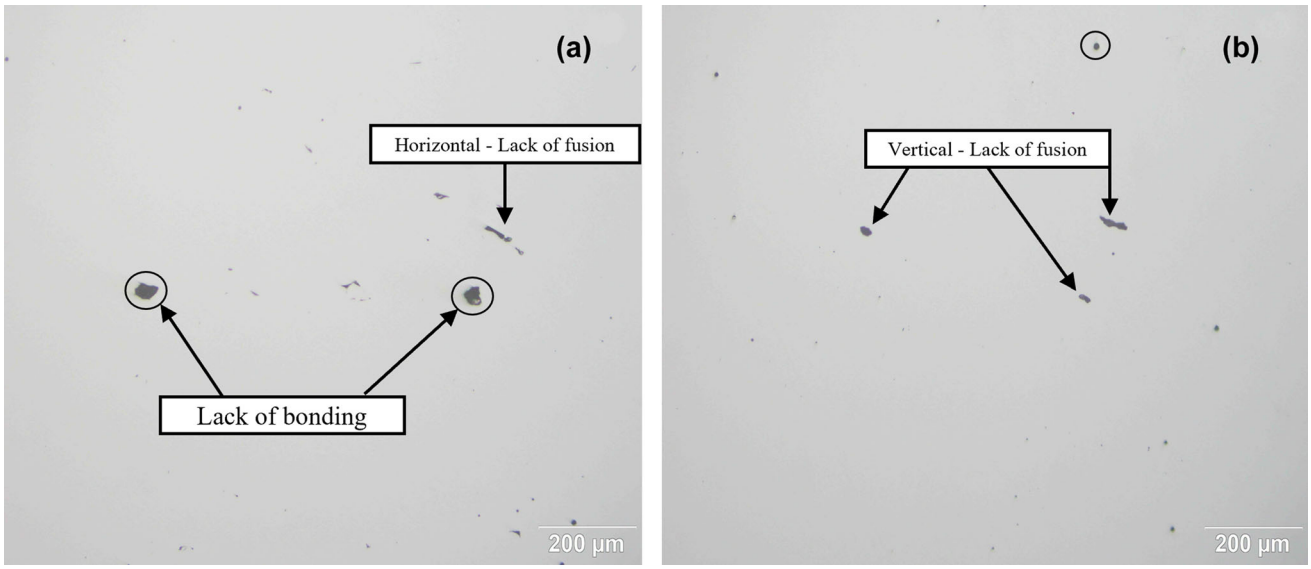

Fig. 4 Optical photomicrographs of samples showing (a) H-LOF in XY Plane and (b) V-LOF in XZ Plane. Circles in both (a) and (b) show lack of bonding between powder particles

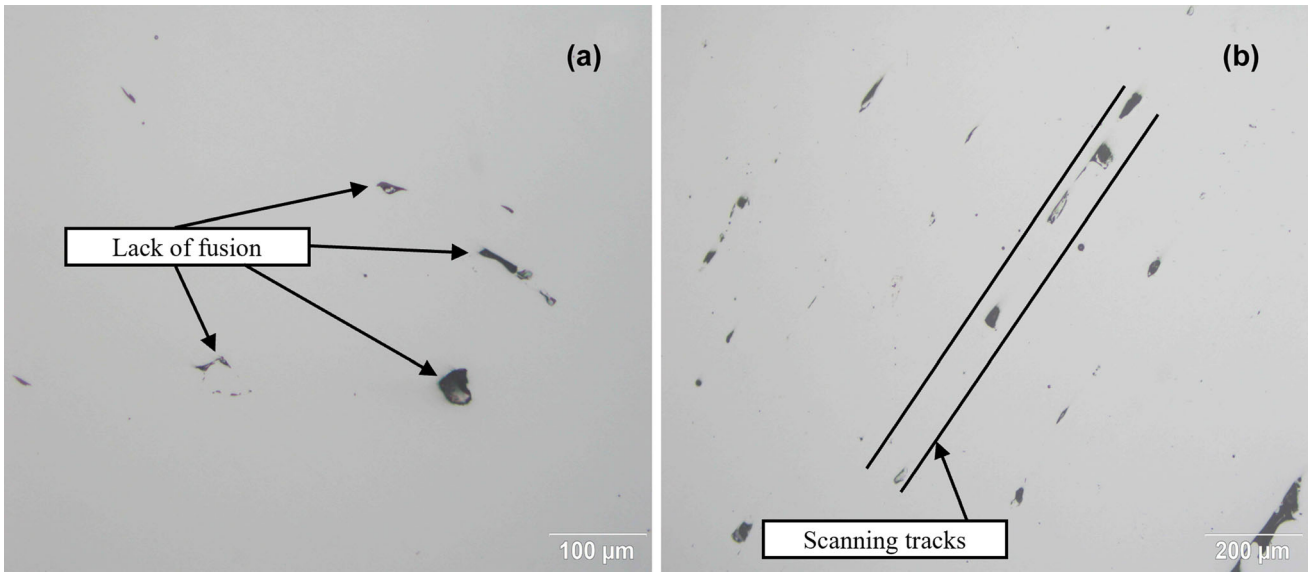

Fig. 5 Optical photomicrographs of samples showing (a) LOF in XY Plane and (b) LOF in scanning track

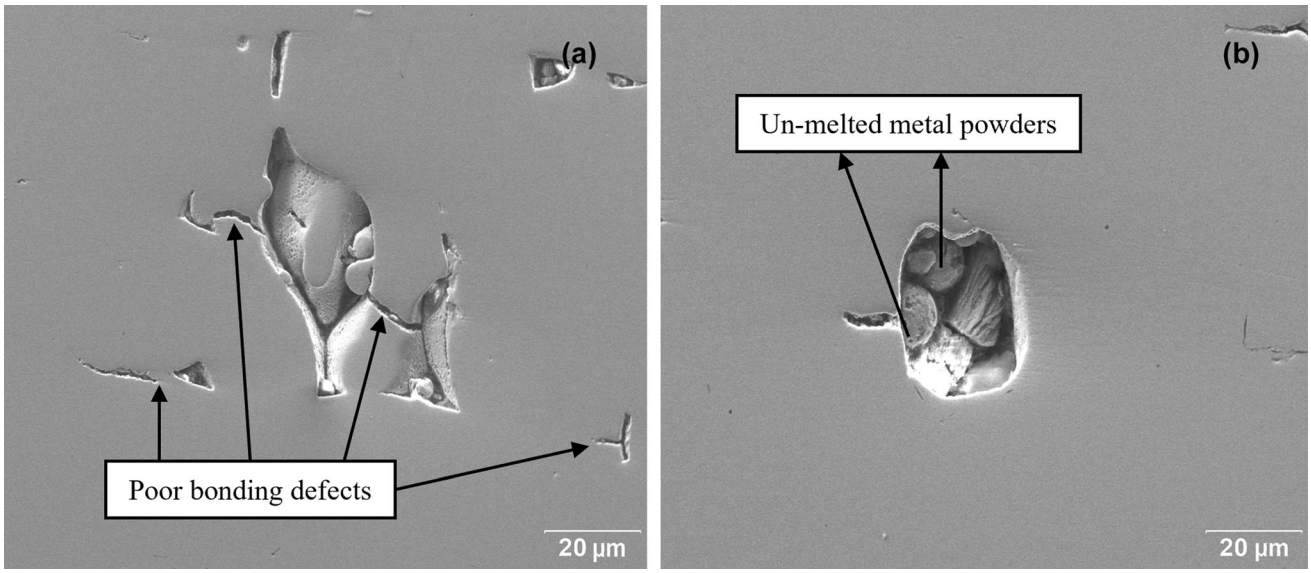

Fig. 6 Scanning electron micrographs of LOF defects (a) due to poor bonding and (b) un-melted metal powders

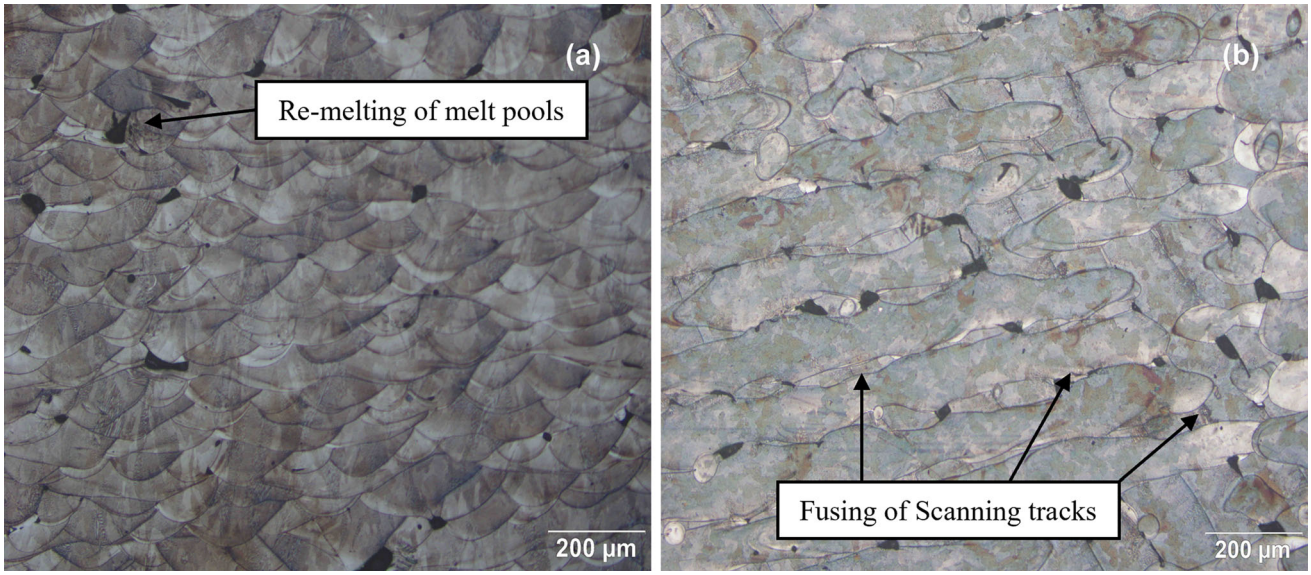

Fig. 7 Optical photomicrographs showing LOF defects formed by deficiency in (a) remelting of melt pools and (b) fusing of scanning tracks

estimating the performance responses to the specific L-PBF process parameters.

A data-driven model has been proposed to predict the densification behavior of L-PBF IN718 alloy for process parameters, *P*, SS and HD. The SS is the most influential process parameter, whereas hatch distance is ranked lowest in terms of percentage contribution. Detailed analysis of defects noticed in metallographically polished and etched specimens has helped in identifying the formation mechanisms of commonly seen defects in L-PBF IN718. This study has brought out a complete understanding on the densification and the effect of L-PBF process parameters on the generation of microscopic defects. Defects being a major disadvantage of AM processed parts, studies on their formation have brought significant clarity in selecting process parameters.

Figure 10(a) and (b) shows the hardness contour plots with laser power and scan speed. The maximum hardness is at 280 W laser power and 960 mm/s scan speed. In XZ and XY planes (Fig. 10) at 320 W laser power (*P*), the hardness increases with scanning speed (SS) up to 960 mm/s and then after decreases.

Hardness can be defined as the resistance of a material to localized plastic deformation. In order to ensure reliability and repeatability of mechanical properties the 3D printed parts, process parameters must be optimized. According to Babu et al., (Ref 42, 43) directional cooling results in anisotropic mechanical properties in AM products. The hardness of sample in as printed condition need not be uniform due to the effect of multiple process parameters involved in additive manufacturing such as laser scan power, scan speed and hatch distance. However, on solution treatment followed by artificial aging (as per AMS 5662 specification for IN718), uniformity can be improved in mechanical properties.

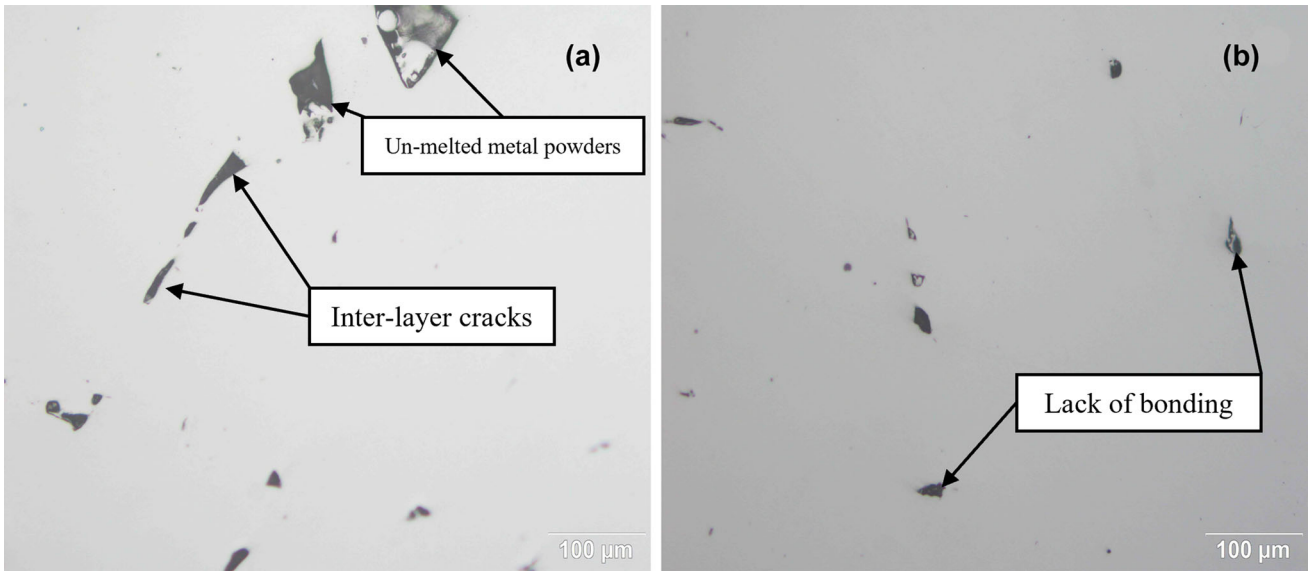

Fig. 8 Optical photomicrographs of inter-layer cracks (a) between two fusion layers and (b) lack of bonding

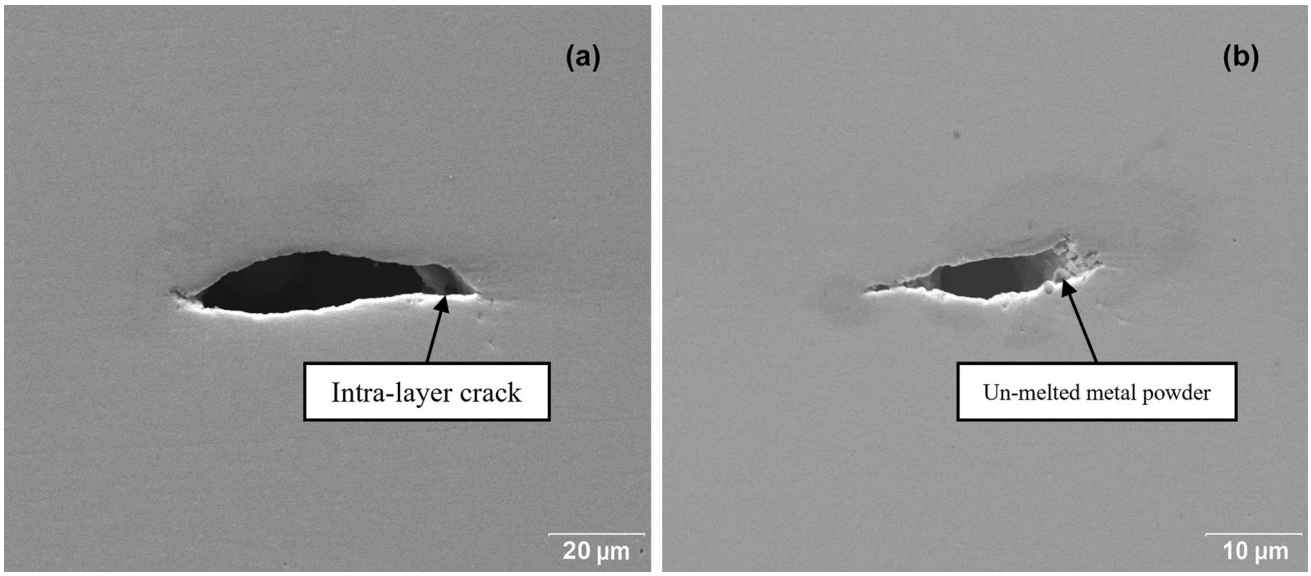

Fig. 9 Scanning electron micrographs of intralayer cracks (a) between solidified layer and the layer being printed and (b) un-melted metal powder

Table 13 Defects identified in samples at different L-PBF process parameters (constant hatch distance, HD = 0.11 mm and layer thickness, LT = 0.04 mm)

L-PBF process parameters			Density, g/cc		
Laser power, *P* (W)	Scanning speed, SS (mm/s)	VED, J/mm^3	Test	Range	Defects
400	300	303.03	7.772	7.663-7.772	Porosity
240	1400	38.96	8.050	7.975-8.085	Lack of fusion
400	1400	64.93	8.080	8.020-8.129	Cracks

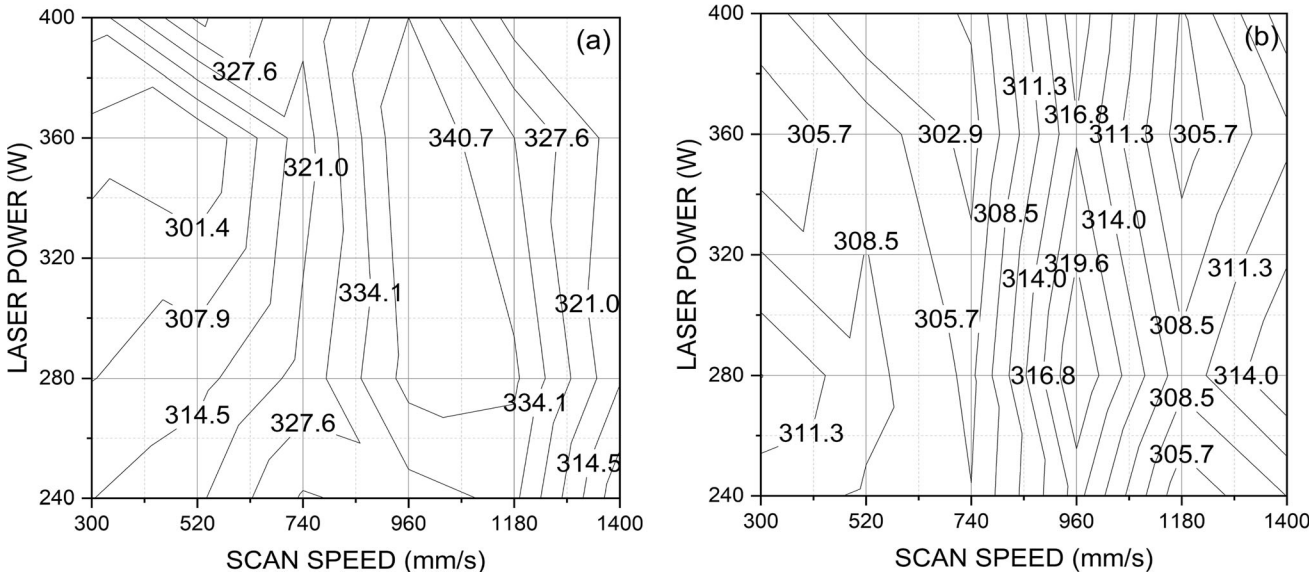

Fig. 10 Contour plot showing variation of hardness in (a) XZ plane and (b) XY plane

5. Conclusions

In modern L-PBF systems, various processing parameters play a crucial role. The key parameters commonly considered include laser power, scanning speed, layer thickness and hatch distance. These parameters are optimized through empirical methods to achieve several objectives such as producing dense materials, minimizing defects, enhancing build speed, reducing surface roughness, and obtaining parts with satisfactory material properties.

Based on extensive experimental trials and analysis of the IN718 data using modified Taguchi approach, the following conclusions are drawn:

1. The optimized L-PBF process parameters for IN718 are $P = 320$ W, SS = 850 mm/s and HD = 0.11 mm, for which the hardness is 334 Hv.
2. Defects such as LOF and un-melted tracks were noticed at low VED values whereas porosity was associated with high VED. Cracks are most evident in XZ plane, and the formation of such cracks is high at high P and SS.
3. Even though, energy density represents the energy input to the process, the findings of this paper conclude that energy density should no longer be considered as a dependent process parameter, as it provides multiple results for the specified energy density.

Acknowledgment

The first author (Kurre Prasanth Kumar Reddy) would like to acknowledge "KLEF-2102070002" full time fellowship awarded for successful completion of the work.

References

1. T.A. Rodrigues, F.W.C. Farias, A. Kaiping Zhang, J.S. Shamsolhodaei, N. Zhou, N. Schell, E. Jan Capek, T.G. Polatidis, and J.P.O. Santos, Wire and Arc Additive Manufacturing of 316L Stainless Steel/Inconel 625 Functionally Graded Material: Development and Characterization, *J. Mater. Res. Technol.*, 2022, **21**, p 237–251. https://doi.org/10.1016/j.jmrt.2022.08.169
2. S. Li, J.Y. Li, Z.W. Jiang, Y. Cheng, Y.Z. Li, S. Tang, J.Z. Leng, H.X. Chen, Y. Zou, Y.H. Zhao, J.P. Oliveira, Y. Zhang, and K.H. Wang, Controlling the Columnar-to-Equiaxed Transition during Directed Energy Deposition of Inconel 625, *Addit. Manuf.*, 2022, **57**, p 102958
3. M. Alizadeh-Sh, S.P.H. Marashi, E. Ranjbarnodeh, R. Shoja-Razavi, and J.P. Oliveira, Prediction of Solidification Cracking by an Empirical-Statistical Analysis for Laser Cladding of Inconel 718 Powder on a Non-Weldable Substrate, *Opt. Laser Technol.*, 2020, **128**, p 106244
4. S. Sanchez, P. Smith, Z. Xu, G. Gaspard, C.J. Hyde, W.W. Wits, I.A. Ashcroft, H. Chen, and A.T. Clare, Powder Bed Fusion of Nickel-Based Superalloys: A Review, *Int. J. Mach. Tools Manuf.*, 2021, **165**, p 103729
5. V. Praveen Kumar and A. Vinoth Jebaraj, Microscale Investigations on Additively Manufactured Inconel 718: Influence of Volumetric Energy Density on Microstructure Texture Evolution, Defects Control and Residual Stress, *Appl. Phys. A Mater. Sci. Process.*, 2023, **129**(5), p 1–17. https://doi.org/10.1007/S00339-023-06642-W/FIGURES/14
6. M. Badrossamay, A. Rezaei, E. Foroozmehr, A. Maleki, and A. Foroozmehr, Effects of Increasing Powder Layer Thickness on the Microstructure, Mechanical Properties, and Failure Mechanism of IN718 Superalloy Fabricated by Laser Powder Bed Fusion, *Int. J. Adv. Manuf. Technol.*, 2022, **118**(5), p 1703–1717. https://doi.org/10.1007/s00170-021-07719-7
7. A. Rosochowski, L. Olejnik, and M. Rosochowska, Tailored Sheared Blanks Produced by Incremental ECAP, *Key Eng. Mater.*, 2015, **651–653**, p 651–656. https://doi.org/10.4028/WWW.SCIENTIFIC.NET/KEM.651-653.651
8. S.V.S. Narayana Murty and B. Nageswara Rao, On the Development of Instability Criteria during Hotworking with Reference to IN 718, *Mater. Sci. Eng. A*, 1998, **254**(1–2), p 76–82. https://doi.org/10.1016/S0921-5093(98)00764-3
9. M. Godec, S. Malej, D. Feizpour, Č Donik, M. Balažic, D. Klobčar, L. Pambaguian, M. Conradi, and A. Kocijan, Hybrid Additive Manufacturing of Inconel 718 for Future Space Applications, *Mater. Charact.*, 2021, **172**, p 110842. https://doi.org/10.1016/j.matchar.2020.110842
10. A. Haghighi, Smart Process-Aware Tolerance Design and Quality Assurance for Additive and Hybrid Manufacturing, University of Illinois at Chicago, 2020
11. L. Scime and J. Beuth, Melt Pool Geometry and Morphology Variability for the Inconel 718 Alloy in a Laser Powder Bed Fusion Additive Manufacturing Process, *Addit. Manuf.*, 2019, **29**, p 100830

12. S. Mannan and B. Puckett, "Physical Metallurgy of Alloys 718, 925, 725, and 725HS for Service in Aggressive Corrosion Environments," *CORROSION 2003*, 2003, p NACE-03126
13. F. Caiazzo, V. Alfieri, and G. Casalino, On the Relevance of Volumetric Energy Density in the Investigation of Inconel 718 Laser Powder Bed Fusion, *Materials*, 2020, **13**(3), p 538. https://doi.org/10.3390/ma13030538
14. J.P. Oliveira, A.D. LaLonde, and J. Ma, Processing Parameters in Laser Powder Bed Fusion Metal Additive Manufacturing, *Mater. Des.*, 2020, **193**, p 108762
15. T. DebRoy, H.L. Wei, J.S. Zuback, T. Mukherjee, J.W. Elmer, J.O. Milewski, A.M. Beese, A. Wilson-Heid, A. De, and W. Zhang, Additive Manufacturing of Metallic Components – Process, *Struct. Prop. Prog. Mater. Sci.*, 2018, **92**, p 112–224. https://doi.org/10.1016/J.PMATSCI.2017.10.001
16. H.Z. Jiang, Z.Y. Li, T. Feng, P.Y. Wu, Q.S. Chen, Y.L. Feng, S.W. Li, H. Gao, and H.J. Xu, Factor Analysis of Selective Laser Melting Process Parameters with Normalised Quantities and Taguchi Method, *Opt. Laser Technol.*, 2019, **119**, p 105592. https://doi.org/10.1016/j.optlastec.2019.105592
17. P. Ferro, R. Meneghello, G. Savio, and F. Berto, A Modified Volumetric Energy Density-Based Approach for Porosity Assessment in Additive Manufacturing Process Design, *Int. J. Adv. Manuf. Technol.*, 2020, **110**(7–8), p 1911–1921. https://doi.org/10.1007/S00170-020-05949-9/TABLES/2
18. Z. Sun, X. Tan, S.B. Tor, and W.Y. Yeong, Selective Laser Melting of Stainless Steel 316L with Low Porosity and High Build Rates, *Mater. Des.*, 2016, **104**, p 197–204. https://doi.org/10.1016/j.matdes.2016.05.035
19. J. Ciurana, L. Hernandez, and J. Delgado, Energy Density Analysis on Single Tracks Formed by Selective Laser Melting with CoCrMo Powder Material, *Int. J. Adv. Manuf. Technol.*, 2013, **68**(5–8), p 1103–1110. https://doi.org/10.1007/S00170-013-4902-4/METRICS
20. K.G. Prashanth, S. Scudino, T. Maity, J. Das, and J. Eckert, Is the Energy Density a Reliable Parameter for Materials Synthesis by Selective Laser Melting?, *Mater. Res. Lett.*, 2017, **5**(6), p 386–390. https://doi.org/10.1080/21663831.2017.1299808
21. H.J. Willy, X. Li, Z. Chen, T.S. Herng, S. Chang, C.Y.A. Ong, C. Li, and J. Ding, Model of Laser Energy Absorption Adjusted to Optical Measurements with Effective Use in Finite Element Simulation of Selective Laser Melting, *Mater. Des.*, 2018, **157**, p 24–34. https://doi.org/10.1016/J.MATDES.2018.07.029
22. J.A. Cherry, H.M. Davies, S. Mehmood, N.P. Lavery, S.G.R. Brown, and J. Sienz, Investigation into the Effect of Process Parameters on Microstructural and Physical Properties of 316L Stainless Steel Parts by Selective Laser Melting, *Int. J. Adv. Manuf. Technol.*, 2014, **76**(5), p 869–879. https://doi.org/10.1007/S00170-014-6297-2
23. L.C. Zhang and H. Attar, Selective Laser Melting of Titanium Alloys and Titanium Matrix Composites for Biomedical Applications: A Review, *Adv. Eng. Mater.*, 2016, **18**(4), p 463–475. https://doi.org/10.1002/ADEM.201500419
24. H. Attar, M. Calin, L.C. Zhang, S. Scudino, and J. Eckert, Manufacture by Selective Laser Melting and Mechanical Behavior of Commercially Pure Titanium, *Mater. Sci. Eng. A*, 2014, **593**, p 170–177
25. X. Fang, W. Xia, Q. Wei, Y. Wu, W. Lv, and W. Guo, Preparation of Cu-Cr-Zr Alloy by Laser Powder Bed Fusion: Parameter Optimization, *Microstruct. Mech. Therm. Propert. Microelectron. Appl.*, 2021, **11**(9), p 1410. https://doi.org/10.3390/MET11091410
26. C. Arvieu, C. Galy, E. Le Guen, and E. Lacoste, Relative Density of SLM-Produced Aluminum Alloy Parts: Interpretation of Results, *J. Manuf. Mater. Process.*, 2020, **4**(3), p 83. https://doi.org/10.3390/jmmp4030083
27. P. Ross, Taguchi Techniques for Quality Engineering: Loss Function, Orthogonal Experiments, Parameter and Tolerance Design, 1996, http://www.sidalc.net/cgi-bin/wxis.exe/?IsisScript=AGRIUAN.xis&method=post&formato=2&cantidad=1&expresion=mfn=023554. Accessed 20 Apr 2022
28. K. Rajyalakshmi and B. Nageswara Rao, Expected Range of the Output Response for the Optimum Input Parameters Utilizing the Modified Taguchi Approach, *Multidiscip. Model. Mater. Struct.*, 2019, **15**(2), p 508–522
29. G. Satyanarayana, K.L. Narayana, and B. Nageswara Rao, Optimal Laser Welding Process Parameters and Expected Weld Bead Profile for P92 Steel, *SN Appl. Sci.*, 2019, **1**(10), p 1–11. https://doi.org/10.1007/S42452-019-1333-3/TABLES/8
30. B.V. Dharmendra, S.P. Kodali, and B. Nageswara Rao, Multi-Objective Optimization for Optimum Abrasive Water Jet Machining Process Parameters of Inconel718 Adopting the Taguchi Approach, *Multidiscip. Model. Mater. Struct.*, 2020, **16**(2), p 306–321
31. B.V. Dharmendra, S.P. Kodali, and B. Nageswara Rao, A Simple and Reliable Taguchi Approach for Multi-Objective Optimization to Identify Optimal Process Parameters in Nano-Powder-Mixed Electrical Discharge Machining of INCONEL800 with Copper Electrode, *Heliyon*, 2019, **5**(8), p e02326. https://doi.org/10.1016/j.heliyon.2019.e02326
32. A. Hussein, L. Hao, C. Yan, and R. Everson, Finite Element Simulation of the Temperature and Stress Fields in Single Layers Built Without-Support in Selective Laser Melting, *Mater. Des. (1980–2015)*, 2013, **52**, p 638–647
33. L. Thijs, K. Kempen, J.P. Kruth, and J. van Humbeeck, Fine-Structured Aluminium Products with Controllable Texture by Selective Laser Melting of Pre-alloyed AlSi10Mg Powder, *Acta Mater.*, 2013, **61**(5), p 1809–1819
34. T. Aboulkhair, N. Everitt, I. Ashcroft, and C. Tuck, Reducing Porosity in AlSi 10 Mg Parts Processed by Selective Laser Melting, *Addit. Manuf.*, 2014, **1**, p 77–86
35. D. Gu, Y.C. Hagedorn, W. Meiners, G. Meng, R.J.S. Batista, K. Wissenbach, and R. Poprawe, Densification Behavior Microstructure Evolution, and Wear Performance of Selective Laser Melting Processed Commercially Pure Titanium, *Acta Mater.*, 2012, **60**(9), p 3849–3860
36. H.K. Rafi, N.V. Karthik, H. Gong, T.L. Starr, and B.E. Stucker, Microstructures and Mechanical Properties of Ti6Al4V Parts Fabricated by Selective Laser Melting and Electron Beam Melting, *J. Mater. Eng. Perform.*, 2013, **22**(12), p 3872–3883. https://doi.org/10.1007/S11665-013-0658-0
37. T.A. Rodrigues, V.R. Duarte, R.M. Miranda, T.G. Santos, and J.P. Oliveira, Ultracold-Wire and Arc Additive Manufacturing (UC-WAAM), *J. Mater. Process Technol.*, 2021, **296**, p 117196
38. X. Zuo, W. Zhang, Y. Chen, J.P. Oliveira, Z. Zeng, Y. Li, Z. Luo, and S. Ao, Wire-Based Directed Energy Deposition of NiTiTa Shape Memory Alloys: Microstructure Phase Transformation Electrochemistry, X-ray Visibility and Mechanical Properties, *Addit. Manuf.*, 2022, **59**, p 103115
39. N. Eschner, L. Weiser, B. Häfner, and G. Lanza, Classification of Specimen Density in Laser Powder Bed Fusion (L-PBF) Using in-Process Structure-Borne Acoustic Process Emissions, *Addit. Manuf.*, 2020, **34**, p 101324. https://doi.org/10.1016/J.ADDMA.2020.101324
40. J. Guzmán, R.D.M. Nobre, E.R. Nunes, D.L. Bayerlein, R.B. Falcão, E. Sallica-Leva, J.B.F. Neto, H.R. Oliveira, V.L. Chastinet, and F.J.G. Landgraf, Laser Powder Bed Fusion Parameters to Produce High-Density Ti-53%Nb Alloy Using Irregularly Shaped Powder from Hydride-Dehydride (HDH) Process, *J. Market. Res.*, 2021, **10**, p 1372–1381. https://doi.org/10.1016/J.JMRT.2020.12.084
41. P.R. Zagade, B.P. Gautham, A. De, and T. DebRoy, Scaling Analysis for Rapid Estimation of Lack of Fusion Porosity in Laser Powder Bed Fusion, *Sci. Technol. Weld. Join.*, 2023, **28**(5), p 372–380. https://doi.org/10.1080/13621718.2022.2164830
42. W.J. Sames, F.A. List, S. Pannala, R.R. Dehoff, and S.S. Babu, The Metallurgy and Processing Science of Metal Additive Manufacturing, *Int. Mater. Rev.*, 2016, **61**(5), p 315–360. https://doi.org/10.1080/09506608.2015.1116649
43. W.J. Sames, F. Medina, W.H. Peter, S.S. Babu, and R.R. Dehoff, Effect of Process Control and Powder Quality on Inconel 718 Produced Using Electron Beam Melting. In *8th International Symposium on Superalloy 718 and Derivatives 2014*, Wiley, 2014, p 409–423, https://doi.org/10.1002/9781119016854.CH32